Supplemental Materials for "Monoclinic $EuSn_2As_2$: A Novel High-Pressure Network Structure"

Lin Zhao,[1, 2, *] Changjiang Yi,[1, *] Chang-Tian Wang,[1, 3, *] Zhenhua Chi,[4, *] Yunyu Yin,[1] Xiaoli Ma,[1] Jianhong Dai,[1] Pengtao Yang,[1] Binbin Yue,[5] Jinguang Cheng,[1] Fang Hong,[1] Jian-Tao Wang,[1, 3, 6, †] Yonghao Han,[2, ‡] Youguo Shi,[1, 7, §] and Xiaohui Yu[1, ¶]

1. Beijing National Laboratory for Condensed Matter Physics and Institute of Physics, Chinese Academy of Sciences, Beijing 100190, China

2. State Key Laboratory of Superhard Materials, Jilin University, Changchun 130012, China

3. School of Physical Sciences, University of Chinese Academy of Sciences, Beijing 100049, China

4. Key Laboratory of Materials Physics, Institute of Solid State Physics, HFIPS, Chinese Academy of Sciences, Hefei 230031, China

5. Center for High Pressure Science & Technology Advanced Research, Haidian, Beijing 100094, China

6. Songshan Lake Materials Laboratory, Dongguan, Guangdong 523808, China

7. Center of Materials Science and Optoelectronics Engineering, University of Chinese Academy of Sciences, Beijing 100049, China

E-mail: wjt@aphy.iphy.ac.cn

hanyh@jlu.edu.cn

ygshi@iphy.ac.cn

yuxh@iphy.ac.cn

(1) Computational methods

Our density functional theory (DFT) calculations are performed using the Vienna *ab initio* simulation package [1] with the all-electron projector augmented wave method [2]. The Perdew-Burke-Ernzerhof revised for solids (PBEsol) [3] exchange-correlation functional is adopted for the evaluation of structural and magnetic stability of $EuSn_2As_2$ under pressure. The valence states $5s^26s^25p^64f^7$ for Eu, $5s^25p^2$ for Sn, and $4s^24p^3$ for As are used with the energy cutoff of 700 eV for the plane wave basis set. To match the energy position of Eu 4*f* bands (-1.68 eV below the Fermi level) in the experiments [4], the Hubbard U = 5 eV is used to treat the localized 4*f* electrons of Eu in the DFT+U scheme [5]. The Brillouin-zone sampling is performed using a 9 × 9 × 9 *k*-point grid for α-$EuSn_2As_2$ in a rhombohedral antiferromagnetic (AFM) primitive cell with space group of R-3m (No. 166) and a 6 × 12 × 6 *k*-point grid for β-$EuSn_2As_2$ in a monoclinic AFM primitive cell with space group of *P2/m* (No. 10). The geometries are optimized with symmetry constraints until the remaining atomic forces are less than 10^{-2} eV/Å and the energy convergence criterion is set at 10^{-8} eV. Phonon calculations are performed using the PHONOPY package [6].

Following the reconstruction mechanism of graphite reported by Wang *et al.* [7], in our simulation, to determine the high-pressure structure, we manually manipulate the sliding and connecting patterns between the SnAs layers via a one-layer by one-layer slip mechanism along the in-plane *b* and *c* directions [see Fig. 1(a)]. According to the one-layer by one-layer slip mechanism under pressure, various possible structures are obtained. And then we relax each structure by *ab initio* calculations and compare the simulated XRD patterns with the experimental XRD data. The β-$EuSn_2As_2$ is more stable than α-$EuSn_2As_2$ above 14.3 GPa [see Fig. 1(e)] and the calculated XRD patterns for β-$EuSn_2As_2$ phase are in good agreement with the experimental XRD patterns (see Fig. 3 and Fig. S2). As a result, the new β-$EuSn_2As_2$ phase can be determined. Beside β-$EuSn_2As_2$, the other metastable network structures are not matching the experimental XRD data and are omitted here.

(2) Experimental methods

Sample synthesis: Single crystals of $EuSn_2As_2$ were grown from Sn flux as mentioned in

Ref. [4]. High-purity Eu, Sn, and As are loaded in an alumina crucible and sealed into quartz tube at a ratio of Eu:As:Sn = 1:3:20. The tube was heated to 1273 K, dwelt for 20 h, and then slowly cooled to 973 K. After that the flux was removed by centrifugation, yielding shiny hexagonal crystals in the crucible.

Electronic transport measurements: The *in-situ* electronic transport measurements of $EuSn_2As_2$ under high pressure at low temperature were established by standard four-probe methods in a non-magnetic Cu-Be alloy Bassett-type diamond anvil cell. The culet of the diamond is 300 μm in diameter. A rhenium gasket was pre-compress to 40 μm in thickness and then a sample chamber with diameter 120 μm was drilled in the center. A piece of single crystal $EuSn_2As_2$ with the dimension of about 100×50×10 μm was loaded into the sample chamber with pressure transmitting medium of KBr. The pressure was determined by ruby fluorescence method at room temperature [8]. The high-pressure four-probe electrical resistance measurement was carried out at High-pressure synergetic measurement station of synergetic extreme condition user facility [9].

XRD measurements: The *in-situ* high pressure XRD patterns are collected with a wavelength of 0.6199 Å from beamline 4W2 at Beijing Synchrotron Radiation Facility. $EuSn_2As_2$ powders and a small ruby are loaded into an optical diamond-anvil cell. Silicone oil is used as pressure transmitting medium. CeO_2 is used as the standard sample to calibrate the parameters of detector. The intensity versus diffraction angle 2θ patterns is integrated by using FIT2D software [10]. The XRD data at various high pressures are refined by Rietveld method [11] through Fullprof program package [12].

(3) Crystal structure under ambient and high pressure

The structure of $EuSn_2As_2$ at ambient pressure was characterized by single crystal and powdered XRD at room temperature (see Fig. S1). The XRD patterns on the flat surface of the sample [see Fig. S1(a)] shows sharp (00L) diffraction peaks, indicating the good quality of the grown crystals. In the powdered XRD patterns [see Fig. S1(b)], almost all of the diffraction peaks can be well indexed to rhombohedral structure with space group *R*-3m, except for tiny diffraction peaks which are attributable to the residual Sn flux.

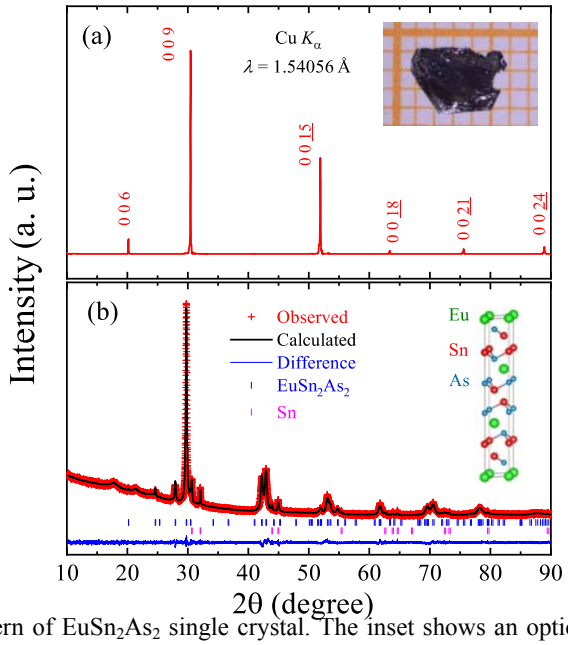

FIG. S1: (a) XRD pattern of $EuSn_2As_2$ single crystal. The inset shows an optical image of $EuSn_2As_2$ single crystal. (b) Refinement of XRD pattern for fine powders grinded from selected $EuSn_2As_2$ single crystals. The inset is a schematic structure for $EuSn_2As_2$ at ambient pressure with space group *R*-3m (No. 166).

(4) Simulated XRD patterns for α- and β-$EuSn_2As_2$

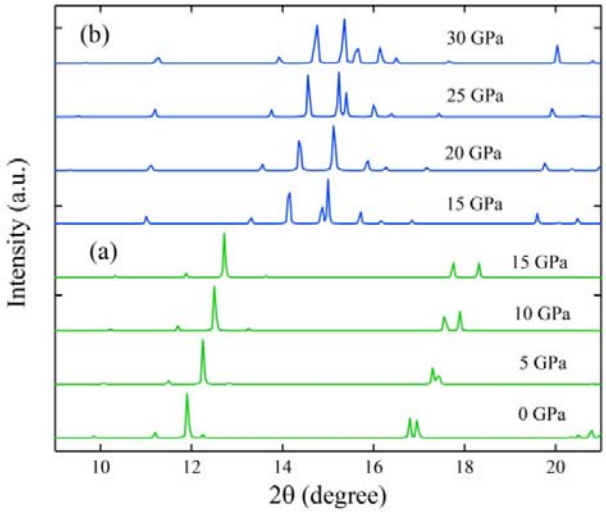

FIG. S2: Simulated XRD patterns with wavelength λ = 0.6199 Å for (a) α-$EuSn_2As_2$ at 0, 5, 10, and 15 GPa; for (b) β-$EuSn_2As_2$ at 15, 20, 25, and 30 GPa.

Figure S2 shows the simulated XRD patterns for α-$EuSn_2As_2$ at 0, 5, 10, and 15 GPa and β-$EuSn_2As_2$ at 15, 20, 25, and 30 GPa. The strongest peaks for α-$EuSn_2As_2$ are located around 12°～13° and 17°～18°. On the other hand, the strongest peaks for β-$EuSn_2As_2$ are located

around 14^{o}～15^{o}. They are all well in agreement with the experimental XRD patterns shown in Fig. 3(a).

(5) The refined lattice parameters, atomic coordinates and Wyckoff positions

For convenient comparison, the experimental XRD patterns obtained at various pressure with wavelength λ = 0.6199 Å are refined by using α-phase (*R*-3m) and β-phase (*C*2/m) as fitting models and the obtained lattice parameters, atomic coordinates and Wyckoff positions (WP) for both α- and β- $EuSn_2As_2$ at various pressures are listed in Table S1.

Table S1: The refined lattice parameters, atomic coordinates and Wyckoff positions (WP).

α-Phase (0.16 GPa)				
Space group: *R*-3m; R_p = 2.61%, R_{wp} = 3.96% *a* = *b* = 4.213 Å, *c* = 26.354 Å, α = 90°, β = 90°, γ = 120°				
atom	*x*	*y*	*z*	WP
Eu	0	0	0	3*a*
Sn	0	0	0.2072	6*c*
As	0	0	0.4066	6*c*
α-Phase (3.7 GPa)				
Space group: *R*-3m; R_p = 2.82%, R_{wp} = 4.47% *a* = *b* = 4.204 Å, *c* = 26.12 Å, α = 90°, β = 90°, γ = 120°				
atom	*x*	*y*	*z*	WP
Eu	0	0	0	3*a*
Sn	0	0	0.2011	6*c*
As	0	0	0.4074	6*c*
α-Phase (9.4 GPa)				
Space group: *R*-3m; R_p = 3.73%, R_{wp} = 4.72% *a* = *b* = 4.122Å, *c* = 24.94Å, α = 90°, β = 90°, γ = 120°				
atom	*x*	*y*	*z*	WP
Eu	0	0	0	3*a*
Sn	0	0	0.2062	6*c*
As	0	0	0.4027	6*c*
α-Phase (11 GPa)				
Space group: *R*-3m; R_p = 4.02%, R_{wp} = 5.05% *a* = *b* = 4.112 Å, *c* = 24.589 Å, α = 90°, β = 90°, γ = 120°				
atom	*x*	*y*	*z*	WP

Eu	0	0	0	3*a*
Sn	0	0	0.2070	6*c*
As	0	0	0.4006	6*c*

α-Phase (15.6 GPa)

Space group: *R*-3m; R_p = 2.44%, R_{wp} = 3.15%
a = *b* = 4.090 Å, *c* = 23.52 Å, *α* = 90°, *β* = 90°, *γ* = 120°

atom	*x*	*y*	*z*	WP
Eu	0	0	0	3*a*
Sn	0	0	0.1994	6*c*
As	0	0	0.4067	6*c*

α-Phase (18.8 GPa)

Space group: *R*-3m; R_p = 2.19%, R_{wp} = 3.11%
a =3.989Å, *b* =3.989 Å, *c* =22.122 Å, *α* = 90°, *β* = 90°, *γ* = 120°

atom	*x*	*y*	*z*	WP
Eu	0	0	0	3*a*
Sn	0	0	0.2046	6c
As	0	0	0.4019	6c

β-Phase (15.6 GPa)

Space group: *C*2/m; R_p = 2.44%, R_{wp} = 3.15%
a =11.183 Å, *b* =3.639 Å, *c* =8.474 Å, *α* = 90°, *β* = 138.9°, *γ* = 90°

atom	*x*	*y*	*z*	WP
Eu	0	0	0	2*a*
Sn	0.6872	0	1.3020	4*i*
As	0.6535	0	0.8397	4*i*

β-Phase (18.8 GPa)

Space group: *C*2/m; R_p = 2.19%, R_{wp} = 3.11%
a =10.928 Å, *b* = 3.474Å, *c* = 8.242Å, *α* = 90, *β* = 138.687°, *γ* = 90°

atom	*x*	*y*	*z*	WP
Eu	0	0	0	2*a*
Sn	0.6745	0	1.2873	4*i*
As	0.6788	0	0.8283	4*i*

β-Phase (27.8 GPa)

Space group: *C*2/m; R_p = 0.661%, R_{wp} = 0.931%
a =10.906 Å, *b* = 3.304Å, *c* = 7.644Å, *α* = 90, *β* = 137.977°, *γ* = 90°

atom	*x*	*y*	*z*	WP
Eu	0	0	0	2*a*
Sn	0.8252	0	1.4166	4*i*
As	0.5899	0	0.8070	4*i*

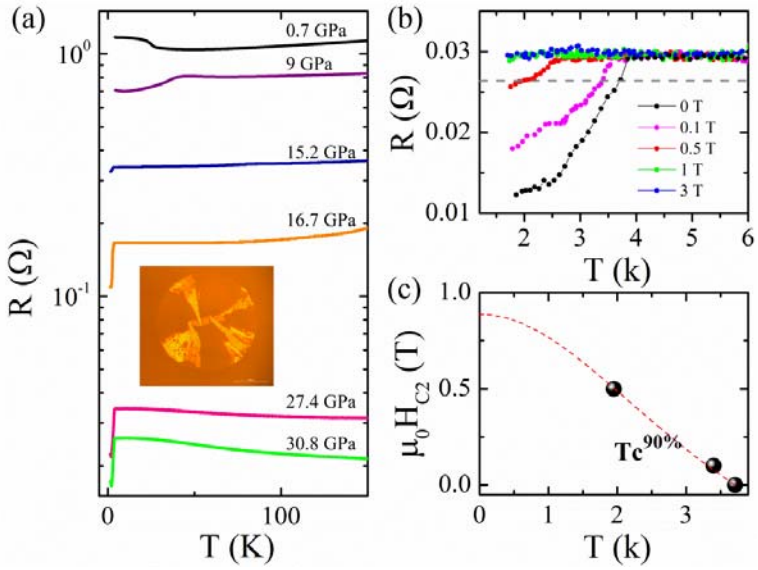

FIG. S3: (a) Temperature dependent resistance of $EuSn_2As_2$ at selected pressures. The inset is a photograph of the measured sample and standard four-probe in DAC chamber. (b) Temperature dependent resistance at 27.4 GPa with various magnetic fields from 0 T to 3 T. (c) Upper critical field versus temperature with extracting 90% of normal resistance. The dashed lines represent the Ginzburg-Landau fits.

(6) Evidence for pressure-induced superconductivity in $EuSn_2As_2$

Figure S3(a) plots the representative R(T) curves of $EuSn_2As_2$ in compression up to 30.8 GPa. With increasing pressure, a superconducting transition with onset temperature $T_C \sim 4$ K is observed at 15.2 GPa [see Fig. 3(c)]. The superconductivity persists up to 30.8 GPa with T_C maintaining a constant value around 4 K. To confirm whether the sudden decrease in resistance around 4 K is superconducting transition or not, we measured the temperature dependent resistance with various external magnetic fields at 27.4 GPa. As shown in Fig. S3(b), the onset transition temperature T_C shifts toward lower temperatures gradually with increasing magnetic fields and then almost fully suppressed when increasing magnetic field to 0.5 T, which can remove the possibility that Sn impurities cause the superconductivity [13,14]. The upper critical fields (H_{C2}) are defined from the drop of 90 % of normal state resistance

(R_n) and plotted in the insert of Fig. S3(c). By using Ginzburg-Landau function as follows [15,16]:

$$\mu_0 H_{C2}(T) = \mu_0 H_{C2}(0) \times (1-T/T_C)^2 / (1+T_C)^2, \quad \text{(S1)}$$

the zero-temperature upper critical field $\mu_0 H_{C2}(0)$ is estimated value of 0.89 T.

(7) Temperature-pressure phase diagram of $EuSn_2As_2$

Based on *in-situ* x-ray diffraction and electrical transport measurements and *ab initio* calculations, we map out a temperature-pressure phase diagram of $EuSn_2As_2$. As shown in Fig. S4, the structural transition from the ambient rhombohedral α-phase (*R*-3m) to monoclinic β-phase (*C*2/m) occurs at 12.6 GPa and accompanied with the emergence of superconductivity at about 15 GPa. The superconductivity remains up to 30.8 GPa with the onset temperature T_C maintaining a constant value ~ 4 K. Accordingly, the structural transition induced by pressure has a remarkable influence on the electrical transport properties. It may help to understand the fundamental relationship between the structure and superconductivity in magnetic topological materials.

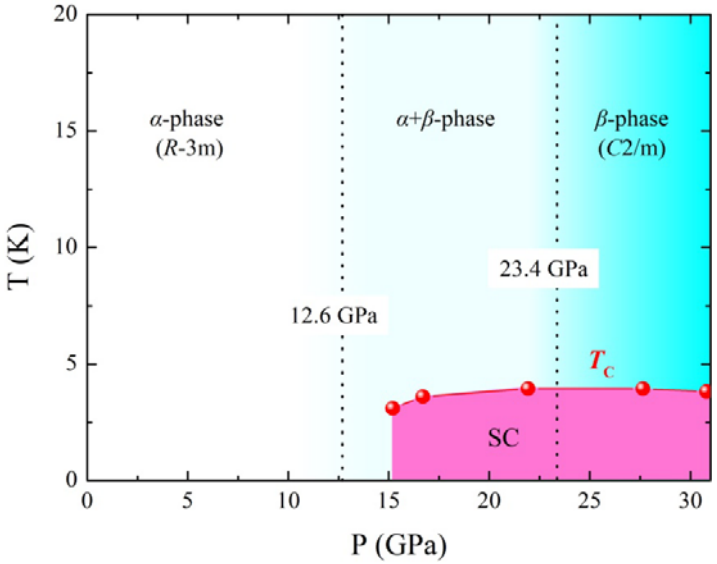

FIG. S4: Temperature-pressure phase diagram of $EuSn_2As_2$. The phase transition from rhombohedral α-phase (*R*-3m) to monoclinic β-phase (*C*2/m) occurs at 12.6 GPa and almost completely achieves around 23.4 GPa. The superconductivity (SC) occurs above 15 GPa with the T_C value of ~ 4 K up to 30.8 GPa.

References

[1] G. Kresse and J. Furthmüller, Phys Rev B. 54, 11169 (1996).

[2] P. E. Blöchl, Phys. Rev. B. **50**, 17953 (1994).
[3] J. P. Perdew, A. Ruzsinszky, G. I. Csonka, O. A. Vydrov, G. E. Scuseria, L. A. Constantin, X. Zhou, and K. Burke, Phys. Rev. Lett. **100**, 136406 (2008).
[4] H. Li, S. Y. Gao, S. F. Duan, Y. F. Xu, K. J. Zhu, S. J. Tian, J. C. Gao, W. H. Fan, Z. C. Rao, J. R. Huang, J. J. Li, Y. Yan, Z. T. Liu, W. L. Liu, Y. B. Huang, Y. L. Li, Y. Liu, G. B. Zhang, P. Zhang, T. Kondo, S. Shin, H. C. Lei, Y. G. Shi, W. T. Zhang, H. M. Weng, T. Qian, and H. Ding, Phys. Rev. X. **9**, 041039 (2019).
[5] V. I. Anisimov, J. Zaanen, and O. K. Andersen, Phys. Rev. B. **44**, 943 (1991).
[6] A. Togo, F. Oba, and I. Tanaka, Phys. Rev. B. **78**, 134106 (2008).
[7] J. T. Wang, C. F. Chen, and Y. Kawazoe, Phys. Rev. Lett. **106**, 075501 (2011).
[8] G. J. Piermarini, S. Block, J. D. Barnett, and R. A. Forman, J. Appl. Phys. **46**, 2774 (1975).
[9] X. H. Yu, F. F. Li, Y. H. Han, F. Hong, C. Q. Jin, Z. He, and Q. Zhou, Chinese Phys. B. **27**, 12 (2018).
[10] A. P. Hammersley, S. O. Svensson, M. Hanfland, A. N. Fitch, and D. Hausermann, High Pressure Res. **14**, 235 (1996).
[11] H. M. Rietveld, J. Appl. Cryst. **2**, 65 (1969).
[12] J. Rodriguezcarvajal, Physica B. **192**, 55 (1993).
[13] A. Eiling and J. S. Schilling, J. Phys. F: Met. Phys. **11**, 623 (1981).
[14] L. D. Jennings and C.A. Swenson, Phys.Rev. **112**, 31 (1958).
[15] X. Li, D. Y. Chen, M. L. Jin, D. S. Ma, Y. F. Ge, J. P. Sun, W. H. Guo, H. Sun, J. F. Han, W. D. Xiao, J. X. Duan, Q. S. Wang, C. C. Liu, R. Q. Zou, J. G. Cheng, C. Q. Jin, J. S. Zhou, J. B. Goodenough, J. L. Zhu, and Y. G. Yao, Proc. Natl. Acad. Sci. U.S.A. **116**, 17696 (2019).
[16] X. C. Pan, X. L. Chen, H. M. Liu, Y. Q. Feng, Z. X. Wei, Y. H. Zhou, Z. H. Chi, L. Pi, F. Yen, F. Q. Song, X. G. Wan, Z. R. Yang, B. G. Wang, G. H. Wang, and Y. H. Zhang, Nat. Commun. **6**, 7804 (2015).